J|A|C|S ARTICLES

Published on Web 02/23/2009

Correlated Dynamics between Protein HN and HC Bonds Observed by NMR Cross Relaxation

Beat Vögeli*,† and Lishan Yao‡

Laboratory of Physical Chemistry, Swiss Federal Institute of Technology, ETH-Hönggerberg, CH-8093 Zürich, Switzerland, and Laboratory of Chemical Physics, National Institute of Diabetes and Digestive and Kidney Diseases, National Institutes of Health, Bethesda, Maryland 20892

Received November 5, 2008; E-mail: beat.voegeli@phys.chem.ethz.ch

Abstract: Although collective dynamics of atom groups steer many biologically relevant processes in biomacromolecules, most atomic resolution motional studies focus on isolated bonds. In this study, a new method is introduced to assess correlated dynamics between bond vectors by cross relaxation nuclear magnetic resonance (NMR). Dipole−dipole cross correlated relaxation rates between intra- and inter-residual H^N-N and $H^\alpha-C^\alpha$ in the 56 residue protein GB3 are measured with high accuracy. It is demonstrated that the assumption of anisotropic molecular tumbling is necessary to evaluate rates accurately and predictions from the static structure using effective bond lengths of 1.041 and 1.117 Å for H^N-N and $H^\alpha-C^\alpha$ are within 3% of both experimental intra- and inter-residual rates. Deviations are matched to models of different degrees of motional correlation. These models are based on previously determined orientations and motional amplitudes from residual dipolar couplings with high accuracy and precision. Clear evidence of correlated motion in the loops comprising residues 10−14, 20−22, and 47−50 and anticorrelated motion in the α helix comprising 23−38 is presented. Somewhat weaker correlation is observed in the β strands 2−4, which have previously been shown to exhibit slow correlated motional modes.

Introduction

Routine NMR approaches to study molecular dynamics assess motions of isolated H−N or H−C bond vectors. ^{15}N relaxation experiments aim at time scales of picoseconds to tens of nanoseconds.[1−3] More recent approaches extend the scale up to milliseconds. Relaxation dispersion studies define time scales of chemical and conformational exchange.[4] Residual dipolar couplings (RDCs)[5] report simultaneously on time averages of bond orientations and motional effects.[6−9] However, it is not trivial to convert relaxation rates or RDCs into amplitudes and directionalities of collective dynamics of groups of atoms with which many biologically relevant processes are associated.[10−12] For example, protein backbone plane motions are mostly reflected in fluctuations around the φ and Ψ backbone angles. Generally, methods to assess relative motions between different bond vectors are required to complete the picture of backbone motion.

In previous studies on protein GB3,[13] highly precise intraresidual H^N-H^α *J*-coupling values have been fitted to Karplus curves to set limits on motions around ϕ angles.[14] Measurements of H^N-H^α RDCs showed that intraresidual values are virtually the same as predicted for a structure exhibiting minimal motion corresponding to $C^\alpha-CO$ fluctuations, whereas sequential values are 9% smaller.[15] Both approaches suggest fluctuations around the ϕ angles to be very small. Furthermore, large sets of RDCs and scalar couplings across hydrogen bonds have been used to identify slow correlated motions in the β sheet.[16] Recently, the motional mode distribution has been reproduced by accelerated molecular dynamics (AMD).[12]

Cross correlated relaxation rates (CCR rates) depend on the relative orientation of two tensorial interactions.[17] In multiple quantum coherences, some of these interactions do not share a common spin and can be located several angstroms apart from one another. CCR rates have been proposed for determination of backbone torsion angles a decade ago by the Griesinger

† Swiss Federal Institute of Technology.
‡ National Institutes of Health.

(1) Lipari, G.; Szabo, A. *J. Am. Chem. Soc.* **1982**, *104*, 4546–4559.
(2) Lipari, G.; Szabo, A. *J. Am. Chem. Soc.* **1982**, *104*, 4559–4570.
(3) Korzhnev, D. M.; Billeter, M.; Arseniev, A. S.; Orekhov, V. Y. *Prog. Nucl. Magn. Reson. Spectrosc.* **2001**, *38*, 197–266.
(4) Kay, L. E. *J. Magn. Reson.* **2005**, *173*, 193–207.
(5) Tjandra, N.; Bax, A. *Science* **1997**, *278*, 1111–1114.
(6) Tolman, J. R.; Al-Hashimi, H. M.; Kay, L. E.; Prestegard, J. H. *J. Am. Chem. Soc.* **2001**, *123*, 1416–1424.
(7) Meiler, J.; Prompers, J. J.; Peti, W.; Griesinger, C.; Bruschweiler, R. *J. Am. Chem. Soc.* **2001**, *123*, 6098–6107.
(8) Peti, W.; Meiler, J.; Bruschweiler, R.; Griesinger, C. *J. Am. Chem. Soc.* **2002**, *124*, 5822–5833.
(9) Yao, L.; Vögeli, B.; Torchia, D. A.; Bax, A. *J. Phys. Chem. B* **2008**, *112*, 6045–6056.
(10) Lindorff-Larsen, K.; Best, R. B.; DePristo, M. A.; Dobson, C. M.; Vendruscolo, M. *Nature* **2005**, *433*, 128–132.
(11) Clore, G. M.; Schwieters, C. D. *J. Mol. Biol.* **2006**, *355*, 879–886.
(12) Markwick, P. R. L.; Bouvignies, G.; Blackledge, M. *J. Am. Chem. Soc.* **2007**, *129*, 4724–4730.
(13) Gronenborn, A. M.; Filpula, D. R.; Essig, N. Z.; Achari, A.; Whitlow, M.; Wingfield, P. T.; Clore, G. M. *Science* **1991**, *253*, 657–61.
(14) Vögeli, B.; Ying, J. F.; Grishaev, A.; Bax, A. *J. Am. Chem. Soc.* **2007**, *129*, 9377–9385.
(15) Vögeli, B.; Yao, L. S.; Bax, A. *J. Biomol. NMR* **2008**, *41*, 17–28.
(16) Bouvignies, G.; Bernado, P.; Meier, S.; Cho, K.; Grzesiek, S.; Bruschweiler, R.; Blackledge, M. *Proc. Natl. Acad. Sci. U. S. A.* **2005**, *102*, 13885–13890.
(17) Goldman, M. *J. Magn. Reson.* **1984**, *60*, 437–452.

10.1021/ja808616v CCC: $40.75

laboratory.[18] Subsequently, a wealth of experiments have been designed to determine the Ψ angle by means of $H^{\alpha}-C^{\alpha}(i)$ dipole/$H^{N}-N(i)$ dipole[18−25] or $H^{\alpha}-C^{\alpha}(i)$ dipole/CO(i) CSA[21,26−28] and the ϕ angle by means of $H^{\alpha}-C^{\alpha}(i-1)$ dipole/$H^{N}-N(i)$ dipole[22,24,25] or $H^{\alpha}-C^{\alpha}$(i-1) dipole/CO(i) CSA[29] CCR rates. Other approaches defining backbone geometry make use of N CSA/CO CSA,[30] $H^{N}-CO$ dipole/$H^{N}-N$ dipole,[30] CO CSA/CO CSA,[31] or $H^{N}-CO$ dipole/CO CSA.[32]

It has been shown that CCR rates are also reporters on dynamics.[33,34] Importantly, in contrast to autorelaxation rates, these rates are sensitive to motion on all time scales.[35,36] Multiple quantum experiments have been proposed to assess backbone plane motion.[37] Sums of $H^{N}-N$ dipole/$CO-C^{\alpha}$ dipole and $H^{N}-C^{\alpha}$ dipole/$CO-N$ dipole[38] or $H^{N}-CO$ dipole/CO CSA[32] CCRs have been interpreted with GAF models.[39,40] $H^{N}-N$ dipole/ $H^{N}-N$ dipole revealed correlated motions in ubiquitin.[35] However, interpretation of dynamics is difficult. Similarly to the interpretation of RDCs, vector orientation and motion are intertwined and generally underdetermined.[7,41] Sensitivity of CCR rates to anisotropy in rotational diffusion[42] complicates the formal description further. A full theoretical description taking into account fast and slow dynamics is still an active field.[36]

In the present study, CCR rates in GB3 are used to study relative fluctuations between $H^{N}-N$ and $H^{\alpha}-C^{\alpha}$ bonds, presumably dominated by the φ and Ψ backbone angles in GB3. Preselected bond orientations are shown to be approximately correct, and deviations from predicted CCR rates are interpreted in terms of motional effects. This approach is opposed to the standard procedure, where dynamics and orientation are fitted simultaneously. The following steps are taken to guarantee highest possible precision and accuracy: (i) Data quality: CCR rates are measured exclusively between dipolar interactions (Figure 1). With a very accurate structure at hand, these rates can be more conveniently evaluated than rates involving CSA interactions. Pulse sequences featuring minimal systematic errors, based on evolution of all multiplet components in multiple quantum coherences, are used to measure CCR rates and are compared to sequences producing a high signal-to-noise ratio, based on direct measurements of interconversion between inphase and antiphase multiple quantum coherences. (ii) Selection of vector orientations: The interpretation crucially depends on the accuracy of the H^{N} and H^{α} proton positions. The orientations of the bond vectors $H^{N}-N$ and $H^{\alpha}-C^{\alpha}$ are taken from a study that employed highly accurate RDCs from multiple alignments.[9] It is shown that these vectors cross-validate best with highly precise $^{3}J_{HNH\alpha}$ scalar couplings and intraresidual and sequential $H^{N}-H^{\alpha}$ RDCs. (iii) Evaluation of the theoretical framework: Models assuming isotropic, axially symmetric, and fully anisotropic tumbling are compared. Examination of the derivation of CCR order parameters is lined out, and values are simulated for different models of motional correlation. Finally, the experimental rates are compared to the simulated rates. Observation of correlated motion in the loops comprising residues 10−14, 20−22, and 47−50 and of anticorrelated motion in the α helix comprising residues 23−38 is supported by 13 ns molecular dynamics (MD) simulations. Somewhat weaker correlation in the β strands 2−4 is not substantiated by the MD simulations.

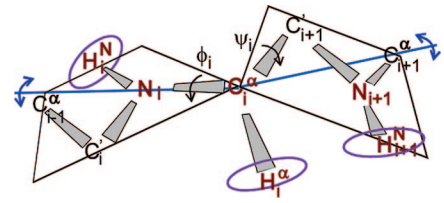

Figure 1. Cartoon representation of bond vectors used in the present study and motions in two peptide backbone planes. Red atoms form the bond vectors of the dipolar mechanism between which CCRs are measured. Pink circles indicate fast bond fluctuation, and the blue arrows represent γ motion about the blue axes in the peptide planes.

Theory

Extraction of Cross-Correlated Relaxation Rates. Evolution of multiple quantum coherence, MQ, between spins I^1 and I^2, where I^1 is weakly scalar coupled to the passive spin S^1 (J_{I1S1}) and I^2 to S^2 (J_{I2S2}) yields eight peaks corresponding to the coherence order (zero and double quantum, ZQ and DQ) and the spin states of S^1 and S^2 (αα, αβ, βα, and ββ). In the secular approximation, magnetization is exchanged between these components by cross-correlated relaxation between six mechanisms (chemical shift anisotropy of I^1 and I^2, and dipolar interaction between I^1-S^1, I^2-S^2, I^1-S^2 and I^2-S^1) resulting in 15 nonuniform contributions to the relaxation rates of the individual peaks.[20] In addition, the nuclear Overhauser effect between S^1 and S^2 must be considered.[23,35] W_0 contributes to the components in the αβ and βα states and W_2 to those in the αα and ββ states. The cross-correlated relaxation rate of interest, $R_{d(I1S1)/d(I2S2)}$, can only be extracted together with other terms from peak intensities I of the components of a ZQ or DQ quadruplet:

(18) Reif, B.; Hennig, M.; Griesinger, C. *Science* **1997**, *276*, 1230–1233.
(19) Yang, D. W.; Kay, L. E. *J. Am. Chem. Soc.* **1998**, *120*, 9880–9887.
(20) Pelupessy, P.; Chiarparin, E.; Ghose, R.; Bodenhausen, G. *J. Biomol. NMR* **1999**, *13*, 375–380.
(21) Chiarparin, E.; Pelupessy, P.; Ghose, R.; Bodenhausen, G. *J. Am. Chem. Soc.* **1999**, *121*, 6876–6883.
(22) Pelupessy, P.; Chiarparin, E.; Ghose, R.; Bodenhausen, G. *J. Biomol. NMR* **1999**, *14*, 277–280.
(23) Reif, B.; Diener, A.; Hennig, M.; Maurer, M.; Griesinger, C. *J. Magn. Reson.* **2000**, *143*, 45–68.
(24) Kloiber, K.; Schuler, W.; Konrat, R. *J. Biomol. NMR* **2002**, *22*, 349–363.
(25) Vögeli, B.; Pervushin, K. *J. Biomol. NMR* **2002**, *24*, 291–300.
(26) Yang, D. W.; Konrat, R.; Kay, L. E. *J. Am. Chem. Soc.* **1997**, *119*, 11938–11940.
(27) Yang, D. W.; Gardner, K. H.; Kay, L. E. *J. Biomol. NMR* **1998**, *11*, 213–220.
(28) Sprangers, R.; Bottomley, M. J.; Linge, J. P.; Schultz, J.; Nilges, M.; Sattler, M. *J. Biomol. NMR* **2000**, *16*, 47–58.
(29) Kloiber, K.; Konrat, R. *J. Biomol. NMR* **2000**, *17*, 265–268.
(30) Pellecchia, M.; Pang, Y. X.; Wang, L. C.; Kurochkin, A. V.; Kumar, A.; Zuiderwegt, E. R. P. *J. Am. Chem. Soc.* **1999**, *121*, 9165–9170.
(31) Skrynnikov, N. R.; Konrat, R.; Muhandiram, D. R.; Kay, L. E. *J. Am. Chem. Soc.* **2000**, *122*, 7059–7071.
(32) Fruh, D.; Chiarparin, E.; Pelupessy, P.; Bodenhausen, G. *J. Am. Chem. Soc.* **2002**, *124*, 4050–4057.
(33) Bruschweiler, R.; Ernst, R. R. *J. Chem. Phys.* **1992**, *96*, 1758–1766.
(34) Daragan, V. A.; Mayo, K. H. *Prog. Nucl. Magn. Reson. Spectrosc.* **1997**, *31*, 63–105.
(35) Pelupessy, P.; Ravindranathan, S.; Bodenhausen, G. *J. Biomol. NMR* **2003**, *25*, 265–280.
(36) Vugmeyster, L.; Pelupessy, P.; Vugmeister, B. E.; Abergel, D.; Bodenhausen, G. *Comptes Rendus Physique* **2004**, *5*, 377–386.
(37) Brutscher, B.; Skrynnikov, N. R.; Bremi, T.; Bruschweiler, R.; Ernst, R. R. *J. Magn. Reson.* **1998**, *130*, 346–351.
(38) Carlomagno, T.; Maurer, M.; Hennig, M.; Griesinger, C. *J. Am. Chem. Soc.* **2000**, *122*, 5105–5113.
(39) Bremi, T.; Bruschweiler, R.; Ernst, R. R. *J. Am. Chem. Soc.* **1997**, *119*, 4272–4284.
(40) Bremi, T.; Bruschweiler, R. *J. Am. Chem. Soc.* **1997**, *119*, 6672–6673.
(41) Tolman, J. R. *J. Am. Chem. Soc.* **2002**, *124*, 12020–12030.
(42) Deschamps, M.; Bodenhausen, G. *ChemPhysChem* **2001**, *2*, 539–543.

$$\frac{1}{4T_{MQ}}\ln\left(\frac{I^{ZQ}_{\alpha\beta}I^{ZQ}_{\beta\alpha}}{I^{ZQ}_{\alpha\alpha}I^{ZQ}_{\beta\beta}}\right) = R_{d(I1S1)/d(I2S2)} + R_{d(I1S1)/d(I2S2)} + R_{d(I1S2)/d(I2S2)} + R_{d(I1S2)/d(I2S2)} + \frac{W_0}{2} - \frac{W_2}{2} \quad (1.1)$$

$$\frac{1}{4T_{MQ}}\ln\left(\frac{I^{DQ}_{\alpha\alpha}I^{DQ}_{\beta\beta}}{I^{DQ}_{\alpha\beta}I^{DQ}_{\beta\alpha}}\right) = R_{d(I1S1)/d(I2S2)} - R_{d(I1S1)/d(I2S1)} - R_{d(I1S2)/d(I2S2)} + R_{d(I1S2)/d(I2S1)} - \frac{W_0}{2} + \frac{W_2}{2} \quad (1.2)$$

T_{MQ} is the constant time during which the coherences evolve. Note that, in both cases, the intensities of the inner components are divided by the outer components (or vice versa, depending on the sign of J_{I1S1} and J_{I2S2}). Unwanted additional contributions are three dipole−dipole cross correlated relaxation rates and half-of W_0 and W_2. However, all terms except for the one of interest depend inversely on the spatial separation of the I^1-S^1 from the I^2-S^2 vector. By identifying I^1 and I^2 with N and C^α, and S^1 and S^2 with the attached protons, $R_{d(I1S1)/d(I2S2)}$ is much larger than the other terms and can be approximately extracted from peak intensities I of the components of a ZQ or DQ quadruplet.[23] In the present application, however, highest possible accuracy and precision are crucial, and the adverse impact of the smaller terms is evaluated. Simulations show that, for intraresidual coherences, $R_{d(I1S1)/d(I2S2)}$, $R_{d(I1S1)/d(I2S1)}$, $R_{d(I1S2)/d(I2S2)}$, and $R_{d(I1S2)/d(I2S1)}$ can be as large as 15, 0.7, 3, and 0.3 s^{-1}, W_0 is typically ≈ 0.3 s^{-1}, whereas W_2 is very small. The contributions to the sequential rates are similar. Clearly, the unwanted terms cannot be neglected, and therefore, the average of the rates obtained from the ZQ and the DQ spectra are used. This is equivalent to using the following:

$$\frac{1}{8T_{MQ}}\ln\left(\frac{I^{ZQ}_{\alpha\beta}I^{ZQ}_{\beta\alpha}I^{DQ}_{\alpha\alpha}I^{DQ}_{\beta\beta}}{I^{ZQ}_{\alpha\alpha}I^{ZQ}_{\beta\beta}I^{DQ}_{\alpha\beta}I^{DQ}_{\beta\alpha}}\right) = R_{d(I1S1)/d(I2S2)} + R_{d(I1S2)/d(I2S1)} \quad (1.3)$$

$R_{d(I1S2)/d(I2S1)}$ cannot be separated from $R_{d(I1S1)/d(I2S2)}$. Although it can be neglected for sequential rates with a typical value of 0.03 s^{-1}, this is not valid for intraresidual rates of typically 0.2 s^{-1}. In the following, both rates must be considered. Under the assumption that radial and spherical motion of the bond vectors are not correlated, the rates are expressed as

$$R_{d(I1S1)/d(I2S2)} = \left(\frac{\mu_0}{4\pi}\right)^2\frac{\gamma_{I1}\gamma_{S1}\gamma_{I2}\gamma_{S2}h^2}{10\pi^2}\frac{1}{(r^{eff}_{I1S1})^3(r^{eff}_{I2S2})^3}J_{d(I1S1)/d(I2S2)}(0) \quad (2.1)$$

$$R_{d(I1S2)/d(I2S1)} = \left(\frac{\mu_0}{4\pi}\right)^2\frac{\gamma_{I1}\gamma_{S1}\gamma_{I2}\gamma_{S2}h^2}{10\pi^2}\frac{1}{(r^{eff}_{I1S2})^3(r^{eff}_{I2S1})^3}J_{d(I1S2)/d(I2S1)}(0) \quad (2.2)$$

where γ_i is the gyromagnetic ratio of nucleus i, r_{ij}^{eff} is the effective distance between nuclei i and j, μ_0 is the permeability of free space, and h denotes Planck's constant. The spectral density function $J_{d(A)/d(B)}(\omega)$ depends on the orientation and dynamics of bond vectors A and B. Equations 2.1 and 2.2 are exact; that is, there are no terms depending on frequencies $\omega \neq 0$.

In the experimental approach presented in Figure 2, all components are minimally manipulated during evolution (referred to as ACE, see NMR spectroscopy), and the peak intensities are obtained from the same spectrum. No invisible systematic errors can be introduced by experimental imperfections such as suboptimal selective pulses. Imperfections rather rescale all components to the same extent and are canceled out in eqs 1.1, 1.2, and 1.3.

Spectral Density Function for Cross-Correlated Relaxation. The correlation function describing dipole/dipole cross-correlated motion between the vectorial tensors A and B can be expressed as the following:[33]

$$C(t) = \frac{4\pi}{5}\sum_{q=-2}^{2}\left\langle\frac{Y^*_{2q}(\theta^{lab}_B(t),\varphi^{lab}_B(t))Y_{2q}(\theta^{lab}_A(0),\varphi^{lab}_A(0))}{r^3_B(t)r^3_A(0)}\right\rangle \quad (3)$$

The angular brackets denote time averages, Y_{2q} are the second rank spherical harmonics, r_X is the length of vector X, and the polar angles θ^{lab} and φ^{lab} orient the vectors in the laboratory frame.

1. Anisotropically Tumbling Rigid Molecule. Generalizing the expressions for the correlation function in ref 3 to the case of cross-correlated relaxation eq 3 can be written as

$$C(t) = \frac{1}{r^3_B r^3_A}\sum_{k=-2}^{2}C_k e^{-t/\tau_k} \quad (4)$$

where $1/\tau_k$ are the eigenvalues of the anisotropic diffusion operator D[43] and the coefficients C_k contain the orientational dependency on the vectors A and B. Explicit expressions for $1/\tau_k$ and C_k are provided in the Supporting Information.

2. Anisotropically Tumbling Dynamic Molecule. In the following, it is assumed that the time dependencies of r and Y_{2q} are not correlated and $\langle 1/r^3_B(t)r^3_A(0)\rangle$ can be expressed with effective bond lengths $1/(r^{eff}_B)^3(r^{eff}_A)^3$.[44] Including fast internal motion requires time averaging of each summand and for the vectors A and B individually in eqs S3.1−5 of the Supporting Information. These modified coefficients may be expressed as $<C_k>$. Lipari and Szabo proposed a single-exponential approximation for C in autorelaxation using an effective correlation time and a generalized order parameter quantifying motion independently of a specific physical model.[1] Ghose et al. extended this approach to cross-correlated relaxation in axially symmetric molecules.[45] Analog application to fully anisotropic tumbling approximates the correlation function as follows:

$$C(t) = \frac{1}{(r^{eff}_B)^3(r^{eff}_A)^3}\sum_{k=-2}^{2}e^{-t/\tau_k}[S^2_k + (C_k - S^2_k)e^{-t/\tau^e}] \quad (5)$$

Here, C_k are functions of the averaged bond orientations. τ^e is the correlation time for internal motion and, the five generalized order parameters individually associated with the eigenvalues are defined as follows:

$$S^2_k \equiv \langle C_k\rangle \quad (6)$$

Even though these order parameters can be very different from one another, a single cross-correlation order parameter has been defined by the sum over all S^2_k.[34]

Fourier transformation of the correlation function gives the spectral density function:

(43) Favro, L. D. *Phys. Rev.* **1960**, *119*, 53–62.
(44) Case, D. A. *J. Biomol. NMR* **1999**, *15*, 95–102.
(45) Ghose, R.; Huang, K.; Prestegard, J. H. *J. Magn. Reson.* **1998**, *135*, 487–499.

$$J(\omega) = \frac{1}{(r_B^{eff})^3 (r_A^{eff})^3} \sum_{k=-2}^{2} \left[\frac{S_k^2 \tau_k}{1 + (\omega\tau_k)^2} + \frac{(C_k - S_k^2)\tau_k^e}{1 + (\omega\tau_k^e)^2} \right] \quad (7)$$

with

$$\frac{1}{\tau_k^e} = \frac{1}{\tau^e} + \frac{1}{\tau_k} \quad (8.1)$$

where τ_k is typically much smaller than the inverse of the Eigenvalues of the diffusion operator D and therefore[45]

$$\frac{1}{\tau_k^e} \approx \frac{1}{\tau^e} + 2\mathrm{tr}(D) \quad (8.2)$$

where "tr" denotes trace. The spectral density function may be written in the same form as used for autorelaxation. C_k must be simply set as a prefactor:

$$J(\omega) = \frac{1}{(r_B^{eff})^3 (r_A^{eff})^3} \sum_{k=-2}^{2} C_k \left[\frac{S_k'^2 \tau_k}{1 + (\omega\tau_k)^2} + \frac{(1 - S_k'^2)\tau_k^e}{1 + (\omega\tau_k^e)^2} \right] \quad (9)$$

where the order parameter S'^2_k is then defined as follows:

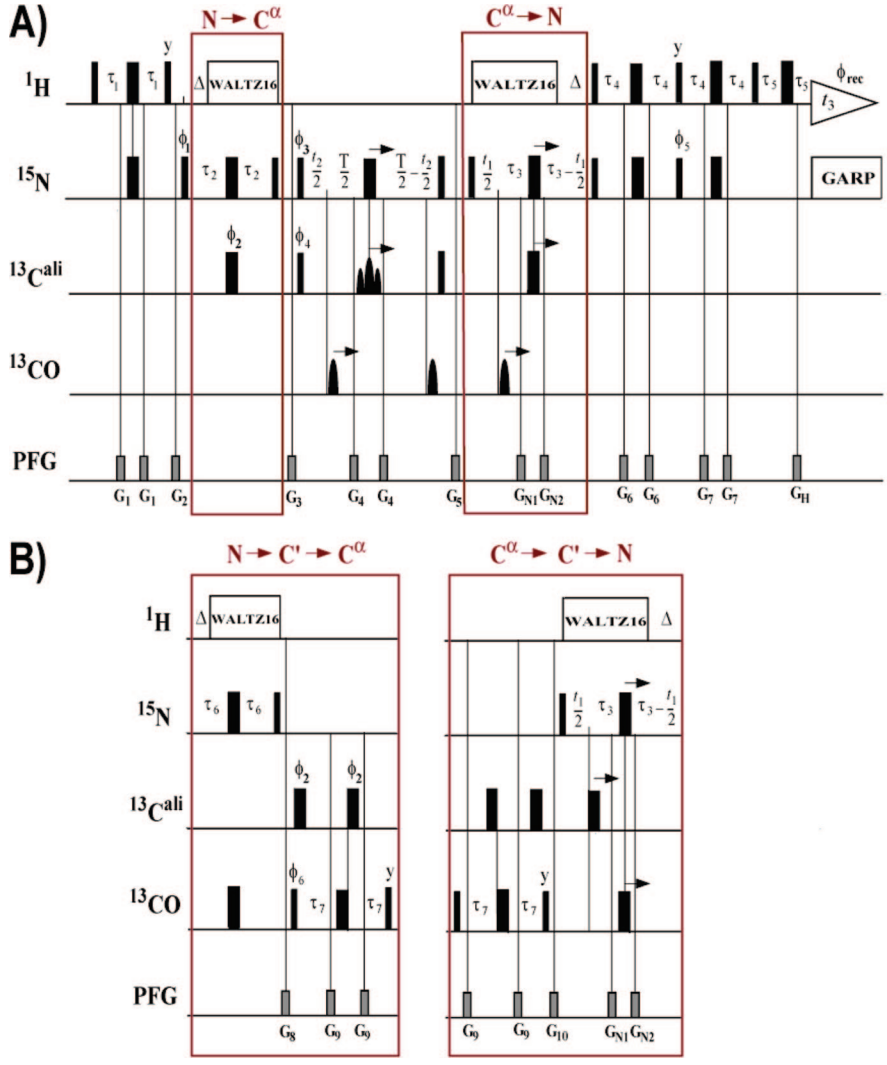

Figure 2. Pulse sequences of the 3D ct-HNCA (A) and ct-HN(CO)CA (B) experiments for intraresidual and sequential $R_{d(HN)/d(H\alpha C\alpha)} + R_{d(H\alpha N)/d(HC\alpha)}$ measurement. For sequence (B), the red boxes in sequence (A) are replaced. The radio frequency pulses on ^{1}H, ^{15}N, $^{13}C^{ali}$, and $^{13}C'$ are applied at 4.7, 118, 56, and 174 ppm, respectively. Narrow and wide bars indicate rectangular 90° and 180° pulses, of which those on ^{13}C are applied with a field of $\Delta/\sqrt{15}$ and $\Delta/\sqrt{3}$, respectively, where Δ is the difference between the $^{13}C^{ali}$ and $^{13}C'$ carriers in hertz. The single curved pulses represent $^{13}C'$-selective 180° sinc pulses of length $p_{C'}{}^{\pi} = 150$ μs, and the triple curved pulse represents a $^{13}C^{\alpha/\beta}$-selective ReBURP pulse[49] of length $p_{C\alpha}{}^{\pi} = 400$ μs applied at 43 ppm. Vertical lines connect centered pulses. ^{1}H-decoupling is achieved with WALTZ16[50] at a field strength γB_1 of 2.1 kHz, and ^{15}N-decoupling is achieved with GARP[51] at a field strength γB_1 of 1.25 kHz. The delays have the following values: $\tau_1 = 2.3$ ms, $\tau_2 = 14$ ms, $\tau_3 = 18$ ms, $\tau_4 = 2.6$ ms, $\tau_5 = 60$ μs, $\tau_6 = 16$ ms, $\tau_7 = 1/(4J_{C\alpha C'}) = 4.5$ ms, $\Delta = 1/(2J_{HN}) = 5.4$ ms, and T/2 = 14.42 ms $- p_{C\alpha}{}^{\pi}/2 - 2(p_{C\alpha}{}^{\pi/2})/\pi$, where $p_{C\alpha}{}^{\pi/2}$ is the length of the rectangular $^{13}C^{ali}$ 90° pulse. Unless indicated otherwise, all radio frequency pulses are applied with phase x. The phase cycle for the (ZQ + DQ) subspectrum is as follows: $\phi_1 = \{x, -x\}$; $\phi_2 = x$; $\phi_3 = \{x, x, x, x, -x, -x, -x, -x\}$; $\phi_4 = \{x, x, -x, -x\}$; $\phi_5 = -y$; $\phi_6 = \{x, x, x, x, x, x, x, x, -x, -x, -x, -x, -x, -x, -x, -x\}$; $\phi_{rec} = \{x, -x, -x, x, -x, x, x, -x\}$for (A) and $\{x, -x, -x, x, -x, x, x, -x, -x, x, x, -x, x, -x, -x, x\}$ for (B). For the (ZQ − DQ) subspectrum, ϕ_3 and ϕ_4 are increased by 90°. Pulsed field gradients indicated on the line marked PFG are applied along the z-axis with duration/strength of the following: G_1, 1200 μs/−9 G/cm; G_2, 2000 μs/12 G/cm; G_3, 2000 μs/12 G/cm; G_4, 100 μs/18 G/cm; G_5, 2000 μs/−15 G/cm; G_{N1}, 200 μs/18 G/cm; G_{N2}, 200 μs/−18 G/cm; G_6, 1200 μs/10.8 G/cm; G_7, 1200 μs/18 G/cm; G_H, 40 μs/−18 G/cm; G_8, 2000 μs/12 G/cm; G_9, 1000 μs/6 G/cm; G_{10}, 2000 μs/12 G/cm. Quadrature detection in the $^{15}N(t_1)$ is achieved by the ECHO-ANTIECHO method[52] applied to ϕ_5 and gradients G_6 and G_7 and in the MQ[^{15}N,$^{13}C^{\alpha}$](t_2) dimension by the States-TPPI method[53] applied to the phases ϕ_2, ϕ_4, and ϕ_{rec}.

$$S'^2_k \equiv \frac{\langle C_k \rangle}{C_k} \tag{10}$$

This order parameter does not meet the Lipari−Szabo criterion anymore[1] but recovers the convenient property that it equals 1 for a perfectly rigid molecule.

3. Symmetrically and Isotropically Tumbling Dynamic Molecule. More convenient expressions are obtained for simpler models: If the molecular tumbling is axially symmetric, $\tau_k = \tau_{-k}$, and eqs 6 and 8.1 can be rewritten as sums over three terms.[34] If the molecular tumbling is isotropic, all τ_k equal the isotropic tumbling time, and the summation is replaced by a single expression:[34]

$$J^{\mathrm{iso}}(\omega) = \frac{1}{(r_{\mathrm{B}}^{\mathrm{eff}})^3 (r_{\mathrm{A}}^{\mathrm{eff}})^3}\left(\frac{S^2\tau}{1+(\omega\tau)^2} + \frac{(\mathrm{P}_2(\cos\theta^{\mathrm{AB}}) - S^2)\tau^e}{1+(\omega\tau^e)^2}\right) \tag{11}$$

The only remaining C coefficient is the Legendre polynomial P_2 of the cosine of the projection angle between the vectors A and B, and the order parameter S^2 is its time average, which is equivalent to the following:

$$S^2 = \frac{4\pi}{5}\sum_{q=-2}^{2} \langle \mathrm{Y}^*_{2q}(\theta_{\mathrm{B}}^{\mathrm{lab}}(t), \varphi_{\mathrm{B}}^{\mathrm{lab}}(t))\rangle \langle \mathrm{Y}_{2q}(\theta_{\mathrm{A}}^{\mathrm{lab}}(t), \varphi_{\mathrm{A}}^{\mathrm{lab}}(t))\rangle \tag{12}$$

Equation 7 reduces to the following:

$$J^{\mathrm{iso}}(\omega) = \frac{\mathrm{P}_2(\cos\theta^{\mathrm{AB}})}{(r_{\mathrm{B}}^{\mathrm{eff}})^3 (r_{\mathrm{A}}^{\mathrm{eff}})^3}\left[\frac{S'^2\tau}{1+(\omega\tau)^2} + \frac{(1-S'^2)\tau^e}{1+(\omega\tau^e)^2}\right] \tag{13}$$

The convenience of the definition in eq 9 is now evident. It has become a standard procedure to relate the experimental spectral density function to that calculated for a rigid molecule by

$$J(\omega) = S^{\mathrm{ah2}} J_{\mathrm{rigid}}(\omega) \tag{14}$$

using an ad hoc order parameter S^{ah2},[25,28,30−32,46,47] which equals S'^2 for isotropic tumbling.

Experimental Section

Sample Expression and Purification. The protein GB3 was expressed and purified as described previously.[48] The ^{13}C-,^{15}N-labeled NMR sample contained 350 μL of 4 mM protein solution in 95% H_2O, 5% D_2O, 50 mM potassium phosphate buffer, pH 6.5, and 0.5 mg/mL sodium azide.

NMR Spectroscopy. The first approach relies on the evolution of all multiplet components of the multiple quantum coherence in a four spin system (see Theory Section). This approach is referred to as "all components evolution" (ACE). The 3D ct-HNCA experiment for measurement of intraresidual $R_{\mathrm{d(HN)/d(H\alpha C\alpha)}} + R_{\mathrm{d(H\alpha N)/d(HC\alpha)}}$ cross-correlated relaxation rates is shown in Figure 2A. $^1H^N(i)$ polarization is excited and converted into multiple quantum coherences MQ[^{15}N(i),$^{13}C^\alpha$(i)] via ^{15}N(i) in two INEPT steps. The MQ coherences are chemical-shift labeled under scalar coupling to $^1H^N(i)$ and $^1H^\alpha(i)$ during $T = 28.84$ ms yielding four components (doublets of doublets) for both the double-quantum and the zero-quantum coherences. Subsequently, the magnetization is converted into single-quantum ^{15}N(i) for chemical shift labeling and transferred back to $^1H^N(i)$ for direct detection. Theoretically, magnetization is also converted into a multiple quantum coherence between ^{15}N(i) and $^{13}C^\alpha(i-1)$, which evolves under scalar coupling to $^1H^N(i)$ and $^1H^\alpha(i-1)$, from which sequential relaxation rates can be extracted. Practically, however, it is not possible to obtain optimal sensitivity simultaneously for intraresidual and sequential coherences, and peak overlap may further limit this approach. Therefore, experiment 2A is used for optimal transfer to intraresidual $^{13}C^\alpha$, whereas signals from sequential coherences are rather weak. Experiment 2B provides exclusively signal from sequential coherences. Magnetization on ^{15}N(i) is transferred to $^{13}C^\alpha(i-1)$ via ^{13}CO(i − 1) with an additional INEPT step (and a second step during the back transfer). This experiment is essentially the one proposed in refs 18 and 23. Two subspectra, (ZQ + DQ) and (ZQ − DQ), are recorded and subsequently added (subtracted) to obtain the ZQ (DQ) spectra. Experimental details are provided in the caption of Figure 2.

Each subspectrum of the 3D ct-HNCA and ct-HN(CO)CA experiments was recorded with $55(t_1) \times 32(t_2) \times 256(t_3)$ complex points, $t_{1\max} = 27.5$ ms, $t_{2\max} = 21.9$ ms, $t_{3\max} = 63.28$ ms, and an interscan delay of 1.0 and 8 scans per increment resulting in a measurement time of 2 days for a pair of subspectra A and B. The time domain data were multiplied with square cosine functions in the direct dimension and cosine functions in the indirect dimensions and zero-filled to 512 × 128 × 2048 complex points.

The approach put forward by the Bodenhausen laboratory is described in detail in the corresponding publications. Two complementary spectra are recorded with peak intensities depending on the interconversion of doubly inphase and doubly antiphase MQ coherences with respect to H^N and H^α. This approach is referred to as "doubly inphase and antihase interconversion" (DIAI). Intraresidual $R_{\mathrm{d(HN)/d(H\alpha C\alpha)}} + R_{\mathrm{d(H\alpha N)/d(HC\alpha)}}$ rates were recorded with a pair of 3D pulse sequences as presented in ref 22 in 2 days. Sequential $R_{\mathrm{d(HN)/d(H\alpha C\alpha)}} + R_{\mathrm{d(H\alpha N)/d(HC\alpha)}}$ were obtained from pairs of 2D pulse sequences as described in ref 20 run for 3 days, or in ref 21 for 1 day.

All experiments were performed on a BRUKER DRX600 MHz spectrometer, equipped with a z-axes gradient cryogenic probe, respectively, at 298 K.

All spectra were processed and analyzed using the software package NMRPipe.[54] Peak heights were determined by parabolic interpolation.

Prediction of CCR Rates. 1. Protein Coordinates Selection. A variety of coordinate sets of GB3 has been deposited in the protein data bank (PDB). In this study, the positions of the H^N and H^α protons are of particular importance. In X-ray structures, protons can be added at idealized positions. However, large sets of RDCs have been used to demonstrate out-of-plane H^N positions.[48] Subsequently, highly accurate RDCs have been used to orient H^N-N and $H^\alpha-C^\alpha$ bond vectors with an iterative DIDC method.[9] $^3J_{\mathrm{HNH\alpha}}$ scalar couplings and intraresidual and sequential $D_{\mathrm{HNH\alpha}}$ RDCs are very sensitive reporters on the proton positions.[14,15] Best cross-validation is obtained with an NMR structure (pdb code: 2OED), where the H^N-N and $H^\alpha-C^\alpha$ bond vectors are replaced by those obtained with the DIDC method. The $H^\alpha-C^\alpha$ vectors obtained from protonated samples as presented in ref 9 and a new set of H^N-N vectors from deuterated samples give the best cross-validation. The bond lengths were scaled to 1.02 and 1.09 Å,

(46) Carlomagno, T.; Felli, I. C.; Czech, M.; Fischer, R.; Sprinzl, M.; Griesinger, C. *J. Am. Chem. Soc.* **1999**, *121*, 1945–1948.
(47) Felli, I. C.; Richter, C.; Griesinger, C.; Schwalbe, H. *J. Am. Chem. Soc.* **1999**, *121*, 1956–1957.
(48) Ulmer, T. S.; Ramirez, B. E.; Delaglio, F.; Bax, A. *J. Am. Chem. Soc.* **2003**, *125*, 9179–9191.
(49) Geen, H.; Freeman, R. *J. Magn. Reson.* **1991**, *93*, 93–141.
(50) Shaka, A. J.; Keeler, J.; Frenkiel, T.; Freeman, R. *J. Magn. Reson.* **1983**, *52*, 335–338.
(51) Shaka, A. J.; Barker, P. B.; Freeman, R. *J. Magn. Reson.* **1985**, *64*, 547–552.
(52) Kay, L. E.; Keifer, P.; Saarinen, T. *J. Am. Chem. Soc.* **1992**, *114*, 10663–10665.
(53) Marion, D.; Ikura, M.; Tschudin, R.; Bax, A. *J. Magn. Reson.* **1989**, *85*, 393–399.
(54) Delaglio, F.; Grzesiek, S.; Vuister, G. W.; Zhu, G.; Pfeifer, J.; Bax, A. *J. Biomol. NMR* **1995**, *6*, 277–293.

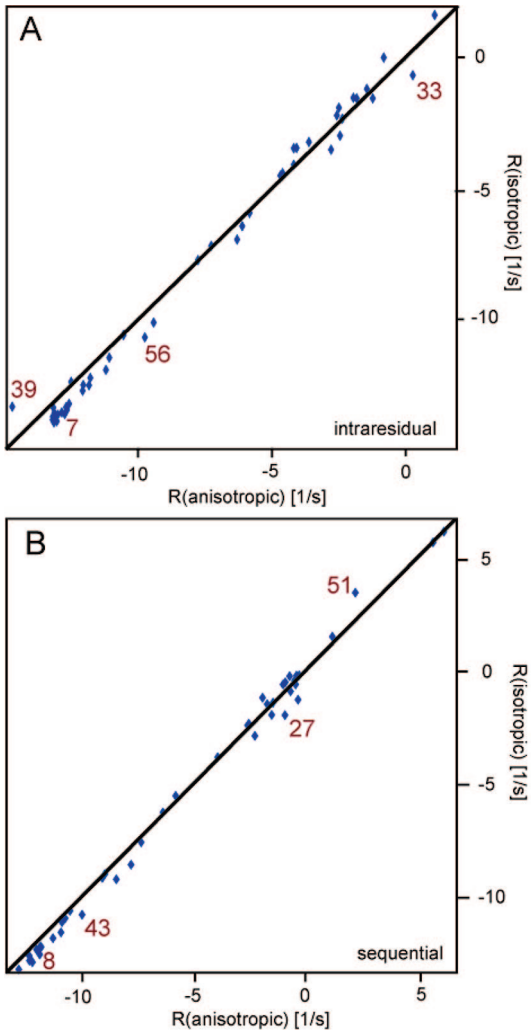

Figure 3. Correlation plot of CCR rates simulated for isotropic and fully anisotropic tumbling of GB3. The protein is assumed to be rigid. $R_{d(HN)/d(H\alpha C\alpha)} + R_{d(H\alpha N)/d(HC\alpha)}$ is abbreviated by R. Diffusion tensors are taken from ref 55. Intraresidual and sequential CCR rates are shown in A and B, respectively. The slopes, obtained by a least-squares fit, are 1.04 and 1.05, and Pearson's correlation coefficients are 0.996 and 0.997, respectively. Residues that show the largest change are marked in red. Pairwise rmsd values are 0.64 and 0.58 s^{-1}.

respectively. Such a coordinate set yields rmsd values between predictions and experimental values of 0.32 Hz for $^3J_{HNH\alpha}$, 1.15 Hz for intraresidual $D_{HNH\alpha}$, and 1.66 Hz for sequential $D_{HNH\alpha}$ with the same alignment strength as in ref 15. Note that all rmsds are lower than in the original publications.

2. Diffusion Model Selection. Very accurate diffusion tensors for GB3 are available from ref 55. The ratio of the main axis to the averaged perpendicular axis is ≈1.4, and there is a small rhombic component. Because of the nonhomogenous distribution of H−N vectors, the effective tumbling time calculated as half the inverse trace of the diffusion tensor is ≈3% larger for the isotropic model than for the nonisotropic ones. $R_{d(HN)/d(H\alpha C\alpha)} + R_{d(H\alpha N)/d(HC\alpha)}$ rates were calculated using eqs 2.1, 2.2, and 7 for isotropic, axially symmetric, and fully anisotropic tumbling. The protein was assumed to be rigid. Correlation plots showing the two extreme cases (isotropic and fully anisotropic) for intraresidual and sequential rates are shown in Figure 3. The slopes indicate an average difference of 4% and 5% with largest changes for residues 7, 33, 39, and 56 and 8, 27, 43, and 51, respectively, for intraresidual and sequential CCR rates.

(55) Hall, J. B.; Fushman, D. *J. Biomol. NMR* **2003**, *27*, 261–275.

3. Order Parameter Modeling. Cross-correlation order parameters are simulated for models with various extents of motional correlation. Amplitudes for H^N-N and $H^\alpha-C^\alpha$ bond motion, σ_{H^NN} and $\sigma_{H^\alpha C^\alpha}$, are obtained from RDC fits assuming Gaussian symmetric motion.[9] Fluctuations of these two bonds around the rotation axis orthogonal to the $N-C^\alpha$ axis are assumed to be uncorrelated in all cases. Correlated, uncorrelated, or anticorrelated motion around the $N-C^\alpha$ axis is expressed as fluctuation of the $H^N-N-C^\alpha-H^\alpha$ dihedral angle:

$$\sigma_{dihed}^{corr} = |\sigma_{H^NN} - \sigma_{H^\alpha C^\alpha}| \quad (15.1)$$

$$\sigma_{dihed}^{uncorr} = \sqrt{\sigma_{H^NN}^2 + \sigma_{H^\alpha C^\alpha}^2} \quad (15.2)$$

$$\sigma_{dihed}^{anticorr} = \sigma_{H^NN} + \sigma_{H^\alpha C^\alpha} \quad (15.3)$$

Order parameters are obtained from eq 10. No distinction between different models of overall tumbling is made, and thus, only integration of the Legendre polynomial of the projection angle is required. Details on the calculation are provided in the Supporting Information. The simplification is justified because the order parameters will be used to estimate corrections to relaxation rates based on a rigid molecule. Such corrections are generally much smaller than the rates themselves. Note that the choice of the axis along which correlated motion is assumed is somewhat arbitrary but runs approximately parallel to the axis of γ motion for both the intraresidual and sequential case (Figure 1).

Molecular Dynamics Simulation. Starting coordinates for the protein atoms were taken from the 2OED structure. The protonation states of the ionizable residues were set to their normal values at pH 7. The protein was solvated by a layer of ~6500 TIP3P[56] water molecules, which extended 12.5 Å from the outermost protein atoms and resulted in a periodic box of the dimensions 52 × 64 × 61 Å. Two Na^+ ions were placed by the Leap program[57] to neutralize the −2 charge of the model system. The parm03 version of the all-atom AMBER force field[58] was used for all the simulations.

MD simulations were carried out using the SANDER module in AMBER 8.0.[57] The SHAKE algorithm was used to constrain the bond lengths of all bonds involving hydrogen atoms permitting a 2 fs time step.[59] A nonbonded pair list with a cutoff of 8.0 Å was updated every 25 steps. The Particle−Mesh−Ewald method was used to include the contributions of long-range electrostatic interactions.[60] The volume and the temperature (300 K) of the system were controlled during the MD simulations (with constant volume) by Berendsen's method.[61]

The simulation time was 14.3 ns with a 1.3 ns equilibration period. Coordinates were saved every 10 ps. All of the MD results were analyzed by using the PTRAJ module of AMBER 8.0 and an in-house program. H^N-N and $H^\alpha-C^\alpha$ order parameters S^2 are calculated using eq 12, and motional amplitudes are extracted under the assumption of Gaussian symmetric motion.

Results and Discussion

Validation of Measurements. 2D planes cut from spectra as obtained in the ACE approach are shown in Figure 4. Residue

(56) Mahoney, M. W.; Jorgensen, W. L. *J. Chem. Phys.* **2000**, *112*, 8910–8922.
(57) Case, D. A.; Cheatham, T. E.; Darden, T.; Gohlke, H.; Luo, R.; Merz, K. M.; Onufriev, A.; Simmerling, C.; Wang, B.; Woods, R. J. *J. Comput. Chem.* **2005**, *26*, 1668–1688.
(58) Duan, Y.; Wu, C.; Chowdhury, S.; Lee, M. C.; Xiong, G. M.; Zhang, W.; Yang, R.; Cieplak, P.; Luo, R.; Lee, T.; Caldwell, J.; Wang, J. M.; Kollman, P. *J. Comput. Chem.* **2003**, *24*, 1999–2012.
(59) Ryckaert, J. P.; Ciccotti, G.; Berendsen, H. J. C. *J. Comput. Phys.* **1977**, *23*, 327–341.
(60) Essmann, U.; Perera, L.; Berkowitz, M. L.; Darden, T.; Lee, H.; Pedersen, L. G. *J. Chem. Phys.* **1995**, *103*, 8577–8593.
(61) Berendsen, H. J. C.; Postma, J. P. M.; Vangunsteren, W. F.; Dinola, A.; Haak, J. R. *J. Chem. Phys.* **1984**, *81*, 3684–3690.

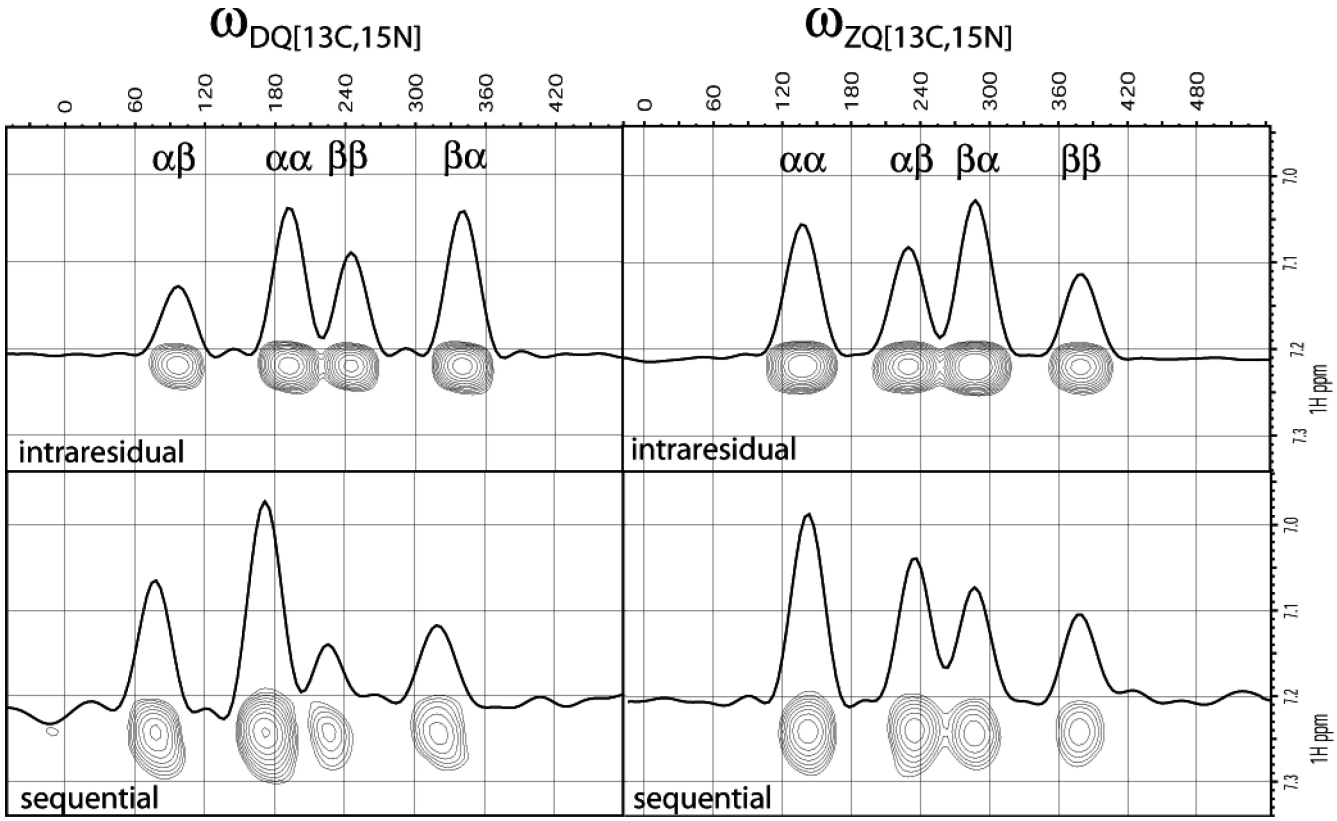

Figure 4. 2D planes and slices cut from the 3D ct-HNCA and ct-HN(CO)CA experiments showing the multiplets of Ala29. DQ spectra are shown on the left and ZQ spectra on the right. Intraresidual multiplets are on top, and sequential multiplets are at the bottom. The horizontal axes represent MQ frequencies in hertz units with arbitrary origins. The peak intensities of residue Ala29 constitute a lower limit for multiplets evaluated.

Ala29 is chosen to represent a lower limit in terms of signal-to-noise. The CCR rates are cross validated with those obtained with the DIAI approach. Relaxation rates obtained from ACE rely on linear combination of relaxation rates of eight individual components (see Theory Section). Equation 1.3 shows that potentially different scaling of peak intensities from the two subspectra is canceled out. Different scaling of the four components from one subspectrum due to additional relaxation pathways, pulse imperfections, and so forth are approximately also eliminated because the MQ evolution is under minimal manipulation. The DIAI experiments suffer from the fact that the ratio of intensities from peaks in two different spectra is calculated. One spectrum serves as a reference and decouples the protons. A second spectrum evolves the MQ coherence into antiphase with respect to both protons that assumes uniform scalar couplings. Undesired pathways superimpose contributions on the evaluated peaks. On the other hand, this approach is very sensitive. The uncertainty of only two (generally strong) peak intensities (as opposed to eight) is propagated, and a smaller random error can be expected. Figure 5 shows correlation plots of experimental $R_{d(HN)/d(H\alpha C\alpha)} + R_{d(H\alpha N)/d(HC\alpha)}$ CCR rates and Table S1 in the Supporting Information lists correlation parameters. The reliability of the ACE approach is demonstrated by the comparison to predicted values (vide infra). In addition, the difference between linear regressions for intraresidual and sequential rates is only 1%. The DIAI approach is not as uniform. By taking the ACE rates as a reference, intraresidual DIAI rates are underestimated by ≈7% with the pulse sequence in ref 22. Interresidual rates are relatively largely overestimated by the initially used pulse sequence[20] (≈20%) but are less than 5% underestimated with an elegantly improved version of the pulse sequence.[21] This observation seems in rough agreement with measurements on human ubiquitin where experimental CCR rates fall on curves predicted for rates with ad hoc order parameters of ≈0.9 and ≈0.76 for the former and latter pulse sequence.[20,21] Note that underestimations of 7% and 5% could hardly be identified using only one experimental approach and no highly accurate structure due to uncertainties in bond vector orientation, tumbling time, and dynamics. Clearly, the slopes of the ACE approach must be used for evaluation of overall order parameters. However, rmsds from predicted values may be comparable or better for DIAI than for ACE. After uniformly scaling all DIAI rates to the slope of ACE, the rmsd between ACE and DIAI rates can be used to estimate the random and a fraction of the systematic error (pairwise rmsd for intraresidual 0.62 s^{-1} and for sequential 0.67 s^{-1}). It should be noted that both approaches might produce some identical systemtic errors, since the two approaches are based on similar principles. Averages of rates from ACE and rescaled rates from DIAI yield errors of about 0.3 s^{-1} (intraresidual 0.31 s^{-1} and sequential 0.34 s^{-1}).

Fit to Rigid Structure. A uniform scaling factor relating predicted to experimental CCR rates is obtained from the slope in a linear regression. This factor is subsequently used to obtain motionally corrected predicted rates, and the pairwise rmsd from the experimental rates is calculated. The data sets in the ACE approach have rmsd values between 0.8 and 1.0 s^{-1}, whereas those from DIAI are between 0.5 and 1.0 s^{-1} (Tables S1 in the Supporting Information). Exceptionally good fits are obtained for the intraresidual DIAI approach, suggesting a low random error. The slopes in the ACE approach differ by 1% for intraresidual and sequential rates, whereas a larger spread is

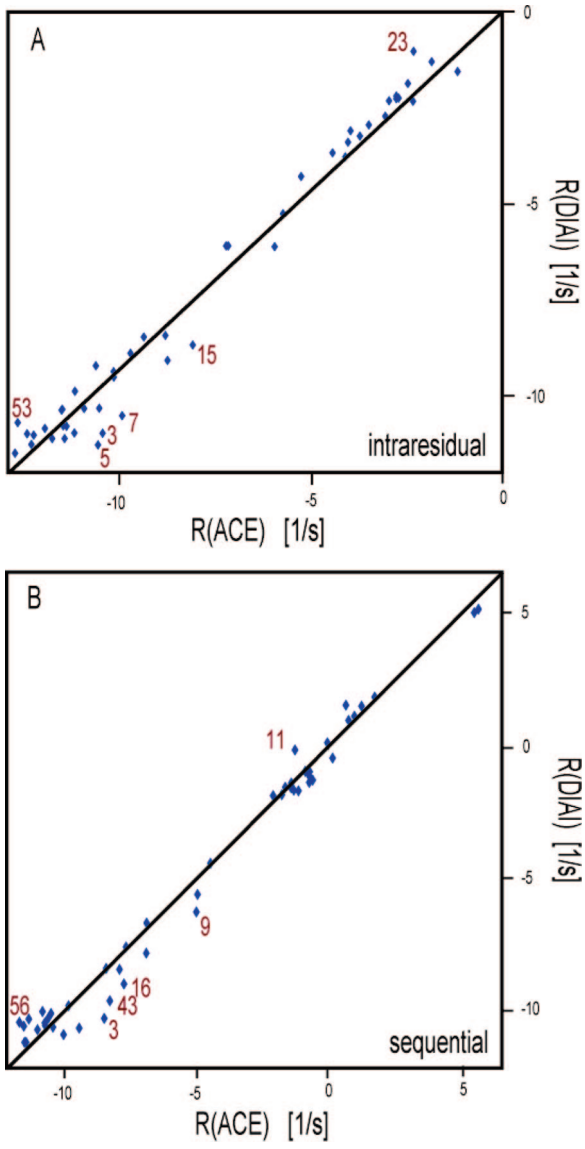

Figure 5. Correlation plots of CCR rates obtained with the ACE and DIAI approaches. $R_{d(HN)/d(H\alpha C\alpha)} + R_{d(H\alpha N)/d(HC\alpha)}$ is abbreviated by R. Intraresidual and sequential CCR rates are shown in A and B, respectively. DIAI rates are scaled to match a slope of 1 (see text) resulting in pairwise rmsd values of 0.62 s^{-1} and 0.67 s^{-1}. Pearson's correlation coefficient is 0.988 and 0.991, respectively. Outliers are marked in red.

obtained in the DIAI approach. Overall, the ACE approach produces a reliable slope, but DIAI proves very sensitive where systematic errors reflected in deficient slopes are mostly uniformly scaled throughout the molecule. In the following, rates obtained from averages of both approaches, where the rates from DIAI are scaled to produce the same slopes as those from ACE are used (Table 1). The change from the isotropic tumbling model to the axially symmetric tumbling model improves the rmsd by ≈0.05 s^{-1}. An additional improvement of ≈0.01 s^{-1} is obtained with the fully anisotropic model. Importantly, choice of the isotropic model yields ≈5% smaller slopes, which would significantly distort the extraction of order parameters. Clearly, the axially symmetric or fully anisotropic model must be used for a proper analysis. Not surprisingly, the small rhombicity of the diffusion tensor has only a small impact on the rmsd and the slope. Figure 6 shows correlation plots of predicted and experimental CCR rates for the anisotropic tumbling model.

As is evident from eqs 6 and 10, S^2 and S'^2 can only be experimentally quantified for isotropic tumbling without invoking a specific model of motion. However, S^{ah2} is model independent and proportional to the slope between the theoretical and experimental CCR rates. Table 1 lists order parameters obtained for all models of molecular tumbling (for a complete list of all experiments see Table S2 in the Supporting Information). Bond lengths r used in the prediction for a rigid molecule are replaced by r^{eff} (see Theory Section). Values of 1.041 and 1.117 Å for H^N-N and $H^\alpha-C^\alpha$ [44], respectively, result in a multiplication factor of 1.144. Such effective lengths absorb radial and angular fluctuations of isolated bonds, that is zero-point librations and vibrations as well as angular fluctuations around the $C^\alpha-C^\alpha$ axis. The isotropic tumbling model produces order parameters that are typically 5% smaller than for the other models. Note that the effective tumbling time is about 3% larger (see Experimental Section) and the additional 2% are effects of nonhomogeneity of the vectors involved in CCR. Deviations of more than 1 s^{-1} are observed for residues 15, 24, 27, 29, 31, and 39 for the intraresidual and 9, 18, 26, 34, 37, 46, and 48 for the sequential rates. Residues 15 (intraresidual) and 46 (sequential) have large errors of 0.62 and 0.48 s^{-1}, respectively, and do fit well using only the DIAI values. These outliers are likely to lack accuracy in the ACE approach. For residues 24, 29, 31, and 39 (intraresidual) and 9, 18, 26, 34, 37, and 48 (sequential), both approaches yield deviation, and for residue 27 (intraresidual), no value could be obtained from the DIAI approach leaving the experimental error unknown. Erroneous vector orientation or dynamic effects may be the cause. However, neither experimental $^3J_{HNH\alpha}$ scalar couplings nor $D_{HNH\alpha}$ RDCs exhibit unusually large deviations from values predicted from the vectors used here (data not shown). Many of these residues are located in the α helix comprising residues 23−36. Generally, few good fits are obtained for the loop with residues 37−41, due to lack of experimental data (residues 38 and 41 are GLY), lack of accurate vector orientation (residue 40), or large deviation (residues 37 and 39). Interestingly, the large deviation for residue 39 is not present when using the isotropic tumbling model (see Figure 3). The only poor fits for β strands are residues 18 (sequential) and 46 (intraresidual). Interestingly, outliers in the α helix fall all to the same side of the slopes.

Overall, the experimental CCR rates can be predicted very closely by setting the order parameter 1 and using effective bond lengths to absorb motional effects. However, these bond lengths are obtained from analysis of motional effects on isolated bonds. In general, their use for prediction of CCR rates is flawed due to presence of correlated motion.

Fit to Dynamic Structures. A more elaborate description of CCR rates takes the presence of correlated motion into account. Therefore, the effective bond length is adjusted to absorb radial but no spherical fluctuation; that is, 1.02 and 1.09 Å are assumed for H^N-N and $H^\alpha-C^\alpha$. It should be noted that, in a recent publication, the effective H^N-N bond length absorbing zero-point vibrations but no angular fluctuations has been determined to be 1.015 ± 0.006 Å. [62] Here, 1.02 Å is chosen, which is frequently used in pdb files and is within the experimental uncertainty range. Order parameters are obtained from integration over projection angles obtained from models assuming uncorrelated, correlated, and anticorrelated bond motion. Figure

(62) Yao, L. S.; Vögeli, B.; Ying, J. F.; Bax, A. *J. Am. Chem. Soc.* **2008**, *130*, 16518–16520.

Table 1. Slopes, Order Parameters, Rmsds, and Pearson's Correlation Coefficient, *r*, between Experimental and Predicted CCR Rates of GB3

CCR	diffusion model[a]	slope[b]	S^{ad2} [c]	S'^2 [c]	rmsd[d] (Hz)	*r*
intraresidual	isotropic	0.849 ± 0.011	0.971 ± 0.013	0.971 ± 0.013	0.75	0.983
	axially symmetric	0.894 ± 0.011	1.023 ± 0.012		0.70	0.986
	fully anisotropic	0.888 ± 0.011	1.016 ± 0.012		0.69	0.986
sequential	isotropic	0.851 ± 0.015	0.973 ± 0.017	0.973 ± 0.017	0.84	0.986
	axially symmetric	0.904 ± 0.014	1.034 ± 0.016		0.74	0.989
	fully anisotropic	0.897 ± 0.014	1.026 ± 0.016		0.73	0.989

[a] The diffusion tensors are taken from ref 55. [b] r_{HN} = 1.02 Å and $r_{H\alpha C\alpha}$ = 1.09 Å are assumed. *X*-axis is the predicted and *Y*-axis the experimental rate. [c] r_{HN}^{eff} = 1.041 Å and $r_{H\alpha C\alpha}^{eff}$ = 1.117 Å are assumed. *X*-axis is the predicted and *Y*-axis the experimental rate. [d] Pairwise rmsd value. The predicted values are multiplied by the slope.

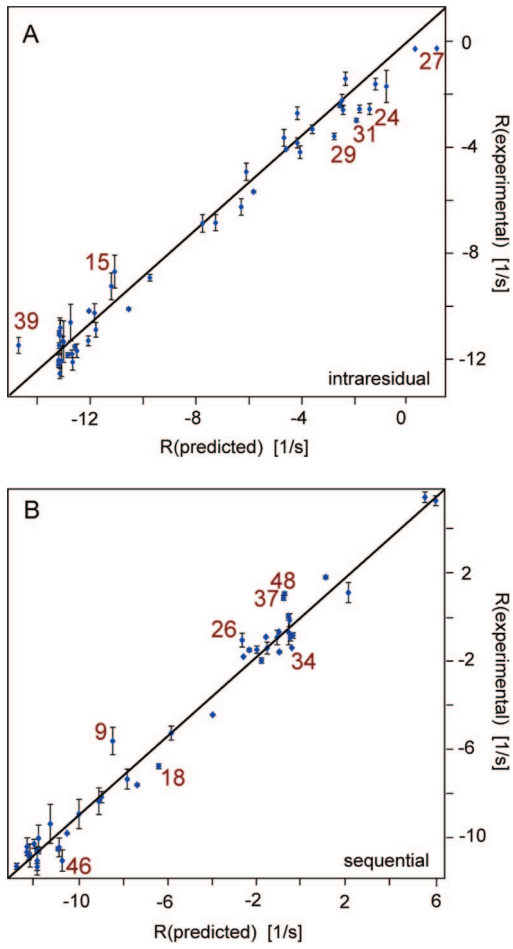

Figure 6. Correlation plots of predicted and experimental CCR rates. $R_{d(HN)/d(H\alpha C\alpha)} + R_{d(H\alpha N)/d(HC\alpha)}$ is abbreviated by R. Intraresidual and sequential CCR rates are shown in (A) and (B), respectively. For prediction, the fully anisotropic model is used.[55] Vertical error bars represent the difference between the values obtained from the ACE and DIAI approaches. The slopes, obtained by a least-squares fit, are 0.888 and 0.897, and Pearson's correlation coefficient is 0.986 and 0.989, respectively. Outliers are marked in red. After scaling the rates obtained from the DIAI approach by the slopes, pairwise rmsd values are 0.69 and 0.73 s^{-1}.

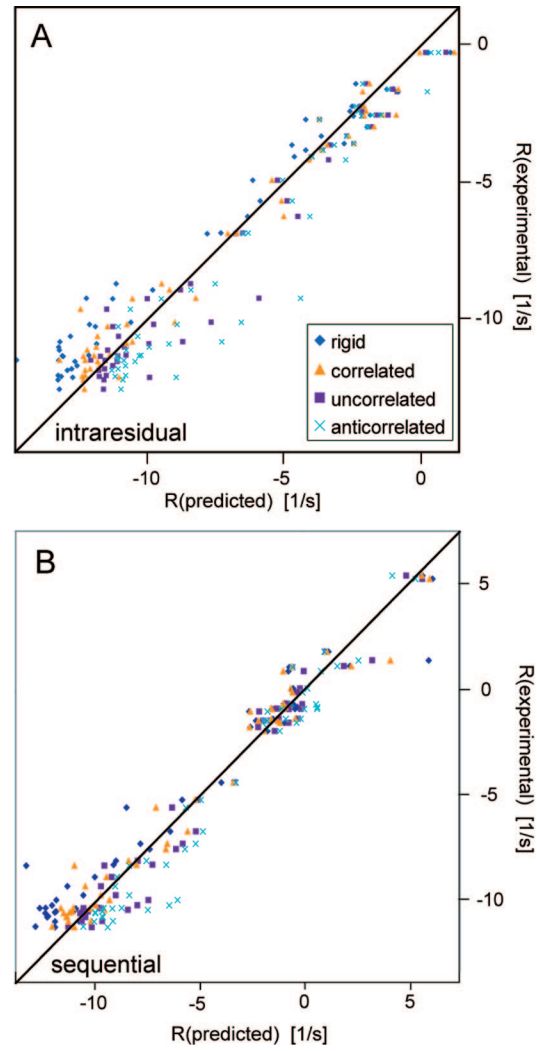

Figure 7. Correlation plots of experimental and predicted CCR rates based on different models for correlated bond motion. $R_{d(HN)/d(H\alpha C\alpha)} + R_{d(H\alpha N)/d(HC\alpha)}$ is abbreviated by R. Intraresidual and sequential CCR rates are shown in (A) and (B), respectively. The theoretical CCR rates are calculated for the rigid molecule (dark blue diamonds) and for models featuring correlated (yellow triangles), uncorrelated (pink squares), and anticorrelated motion (light blue crosses). Bond specific motional amplitudes obtained from H^N-N and $H^\alpha-C^\alpha$ RDCs have been used in eqs 15.1−15.3 to model the extent of motional correlation. Then, order parameters are obtained from integration over the projection angles. The motional model that predicts the value closest to the experimental rate is assigned to each connectivity.

7 shows correlation plots relating the experimental relaxation rates to the simulated relaxation rates for four models of correlated motion: fully correlated motion (equivalent to the rigid molecule), correlated and anticorrelated motion around the $H^N-N-C^\alpha-H^\alpha$ dihedral angle, and uncorrelated motion. Generally, order parameters from anticorrelated motions are the smallest, followed by uncorrelated motion and correlated motion. As expected, the rigid model (complete correlation) overestimates the rates for nearly all residues because shortening effective bond lengths simply rescales the order parameters obtained in the previous section. The prediction closest to the experimental values is about evenly distributed between the three nonrigid models. Some predictions fall clearly outside the experimental error range. The cumulated uncertainties from experimental errors, errors in bond orientation, motional amplitudes of the isolated bonds, and simplification of the models do not allow quantification of correlation degrees. Nevertheless,

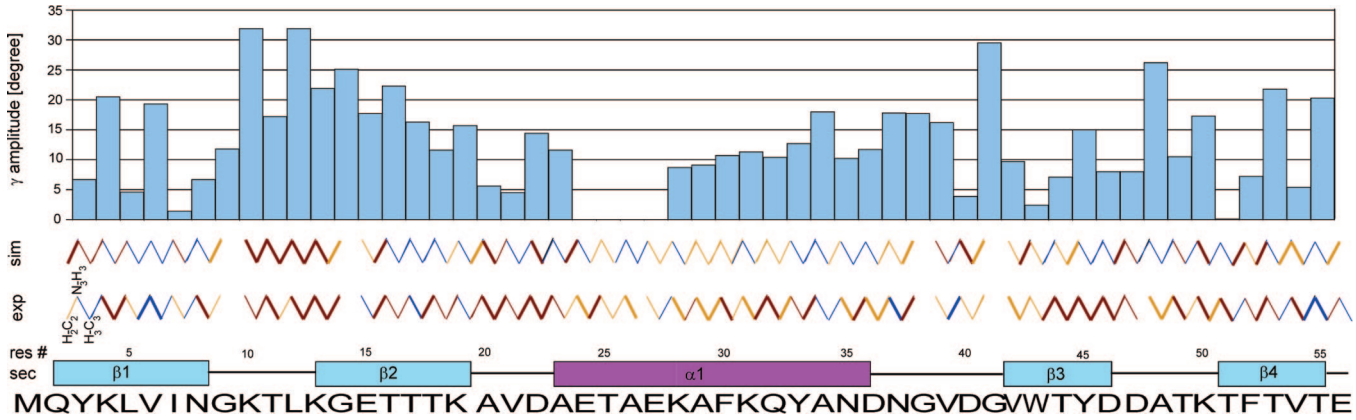

Figure 8. Dynamics correlation network of GB3. $C^{\alpha}_{(i-1)}-N_i$ and $N_i-C^{\alpha}_i$ vectors are color coded according to the best matching model for motional correlation between $H^{\alpha}-C^{\alpha}$ and H^N-N bonds: correlated motion, red; uncorrelated motion, blue; anticorrelated motion, yellow. The network labeled "exp" ("sim") is obtained from the experimental CCR rates (13 ns MD simulation). Bold lines are used if the model assignment is unambiguous within the experimental error range in the experimental approach and if the difference between the dihedral fluctuation and expression 15.2 is larger than 3.5°. On top of the networks, amplitudes of the γ motion presented in ref 16 are plotted.

trends in specific structural elements can be observed. Figure 8 shows the $H^NN-H^{\alpha}C^{\alpha}$ network. The motional model that predicts the value closest to the experimental rate is assigned to each connectivity (For a similar map with model assignment in letter code see Figure S1 in the Supporting Information). In addition, model assignments based on a 13 ns trajectory of a molecular dynamics (MD) simulation are shown. Here, expression 15.2 is subtracted from the rmsd of the dihedral angle. If this value is smaller than −2° (larger than +2°), correlated (anticorrelated) motion is assigned. Experimental evidence of correlated motion in the loops comprising residues 10−14, 20−22, and 47−50 and of anticorrelated motion in the α helix comprising 23−38 is supported by MD simulations. Somewhat weaker correlation in the β strands 2−4 is not substantiated by the MD simulations. Such motion may be present on a time scale not sampled by the simulation but be picked up by RDCs and CCR rates.

Indeed, correlated motion of the β sheet in GB3 in the nano- to millisecond range has been proposed based on measurements of scalar couplings across hydrogen bonds.[16] In this study, Gaussian motional amplitudes in three dimensions but not the degree of correlation have been calculated with large sets of RDCs (see Figure 8). Comparison of RDC order parameters to Lipari−Szabo order parameters and accelerated molecular dynamics (AMD)[12] then indicates microsecond to millisecond motion in the loops and the β sheet but not in the α helix. In the strands β_1, β_3, and β_4, an alternation of large and small motional amplitudes is observed pointing to a mode coupled across the sheet. Interestingly, the pattern matches the alternation of strongly hydrophobic side chains buried in the protein core. Such alternation is not present in the CCR pattern. However, the CCR data does not probe exactly the same type of motion, and a strict comparison has to be handled with care. In addition, the authors proved the presence of correlated motion across the β sheet. For this purpose, scalar couplings across hydrogen bonds simulated for an ensemble exhibiting correlated motion are shown to cross-validate best with the experimental data. Note that such an approach cannot be applied to the α helix and the loops. In the present study, correlated motion is detected within the polypeptide chain. Apparently, the correlated motion of the β sheet undergoes a collective rotational fluctuation along the polypeptide chain in a manner synchronized with neighboring β strands.

In this context, it is interesting to note that supra τ_c motion has also been proposed along the entire sequence of ubiquitin, which has a fold similar to GB3.[63,64] Again, this has been concluded from the observation that RDC orders parameters covering a time window up to milliseconds are smaller than Lipari−Szabo order parameters. A major part of this dynamics is concentrated in a single concerted mode related to molecular recognition.[64] In particular, β strand residues with solvent-exposed side chains exhibit reduced order parameters relative to those with core side chains.[63] This may be a hint to collective motional β sheet behavior on slow time scale.

Conclusion

A new method is introduced to assess correlated dynamics between bond vectors. Cross-correlated relaxation rates are measured with high precision between vectors with accurately known orientation. Experimental rates are compared to rates predicted for a rigid structure. It is demonstrated that the assumption of anisotropic molecular tumbling is necessary to evaluate precisely cross-correlated relaxation rates. Deviations are matched to models of different degrees of motional correlation. These models are based on previously determined orientations and motional amplitudes of isolated bond vectors obtained from residual dipolar couplings. It is shown that for GB3 predictions from a static structure using effective bond lengths absorbing libration and vibration (1.041 and 1.117 Å for H^N-N and $H^{\alpha}-C^{\alpha}$) are within 3% of both experimental intra- and interresidual rates. Analysis involving motional models shows clear evidence of correlated motion in the loops comprising residues 10−14, 20−22, and 47−50 and of anti-correlated motion in the α helix comprising 23−38. Somewhat weaker correlation is observed in the β strands 2−4, which have previously been shown to exhibit slow correlated motional modes. More experimental data and further refinement of motional models are expected to lead toward individual quantification of correlated dynamics between bond vectors.

Acknowledgment. We thank Dr. Ad Bax for valuable discussion. This work was supported by the Intramural Research Program

(63) Lakomek, N. A.; Fares, C.; Becker, S.; Carlomagno, T.; Meiler, J.; Griesinger, C. *Angew. Chem., Int. Ed.* **2005**, *44*, 7776–7778.
(64) Lange, O. F.; Lakomek, N. A.; Fares, C.; Schröder, G. F.; Walter, K. F. A.; Becker, S.; Meiler, J.; Grubmüller, H.; Griesinger, C.; De Groot, B. L. *Science* **2008**, *320*, 1471–1475.

of the NIDDK, NIH, and by the Intramural AIDS-Targeted Antiviral Program of the Office of the Director, NIH.

Supporting Information Available: Full description of the correlation function of an anisotropically tumbling molecule; details on calculation of simulated order parameters; figure showing dynamics correlation network with letter code; table presenting slopes, rmsd values, and Pearson's correlation coefficients between experimental CCR rates; table presenting slopes, order parameters, rmsd values, and Pearson's correlation coefficients between experimental and predicted CCR rates; table presenting experimental and predicted CCR rates. This material is available free of charge via the Internet at http://pubs.acs.org.

JA808616V